Helmholtz-Zentrum Dresden-Rossendorf (HZDR)

HELMHOLTZ ZENTRUM
DRESDEN ROSSENDORF

Electromagnetic probes of a pure-glue initial state in nucleus-nucleus collisions at energies available at the CERN Large Hadron Collider

Vovchenko, V.; Karpenko, I. A.; Gorenstein, M. I.; Satarov, L. M.; Mishustin, I. N.; Kämpfer, B.; Stöcker, H.;

Originally published:

August 2016

Physical Review C 94(2016), 024906

DOI: https://doi.org/10.1103/PhysRevC.94.024906

Perma-Link to Publication Repository of HZDR:

https://www.hzdr.de/publications/Publ-23437

Release of the secondary publication
on the basis of the German Copyright Law § 38 Section 4.

Electromagnetic probes of pure glue initial state in nucleus-nucleus collisions at LHC

V. Vovchenko[1,2,3], Iu. A. Karpenko[1,4], M. I. Gorenstein[1,4],
L. M. Satarov[1,5], I. N. Mishustin[1,5], B. Kämpfer[6,7], and H. Stöcker[1,2,8]

[1] *Frankfurt Institute for Advanced Studies, D-60438 Frankfurt, Germany*

[2] *Johann Wolfgang Goethe Universität, D-60438 Frankfurt, Germany*

[3] *Taras Shevchenko National University of Kiev, 03022 Kiev, Ukraine*

[4] *Bogolyubov Institute for Theoretical Physics, 03680 Kiev, Ukraine*

[5] *National Research Center "Kurchatov Institute", 123182 Moscow, Russia*

[6] *Helmholtz-Zentrum Dresden-Rossendorf, D-01314 Dresden, Germany*

[7] *Technische Universität Dresden, Institut für Theoretische Physik, D-01062 Dresden, Germany*

[8] *GSI Helmholtzzentrum für Schwerionenforschung GmbH, D-64291 Darmstadt, Germany*

Abstract

Partonic matter produced at the early stage of ultrarelativistic nucleus-nucleus collisions is assumed to be composed mainly of gluons, but quarks and antiquarks are produced at later times. The dynamical evolution of this chemically nonequilibrium system is described by the ideal (2+1)–dimensional hydrodynamics with a time dependent (anti)quark fugacity. The equation of state is taken as a linear interpolation of the lattice data for the pure gluonic matter and the chemically equilibrated quark-gluon plasma. The spectra and elliptic flows of thermal dileptons and photons are calculated for central Pb+Pb collisions at the LHC energy. The results are obtained assuming different equilibration times, including the case when the complete chemical equilibrium of partons is reached already at the initial stage. It is shown that a suppression of quarks at early times leads to a significant reduction of the invariant mass spectra of dileptons, but a rather modest suppression of the p_T-distributions of direct photons. It is demonstrated that a noticeable enhancements of photon and dilepton elliptic flows might be a good signature of the pure glue initial state.

PACS numbers: 12.38.Mh, 25.75.-q, 47.75.+f

I. INTRODUCTION

Strongly interacting matter with extremely high energy density can be created in the laboratory at the early stages of relativistic nucleus-nucleus (A+A) collisions. An important physical question is how the nonequilibrium initial system of two nucleon flows from colliding nuclei transforms to a state of quarks and gluons in a local thermodynamic equilibrium, i.e. the quark-gluon plasma (QGP). The initial stage of A+A collisions was described by different theoretical models ranging from simple parton cascades [1, 2], to more sophisticated string-parton models (UrQMD, PHSD) [3–5], color glass condensate [6], coherent chromofields [7, 8], IP-Glasma [9] etc. It is usually assumed that strong nonequilibrium effects take place only during a very short proper time interval $\tau_s \sim 1/Q_s$, where $Q_s \simeq 1 \div 2$ GeV is the so-called gluon saturation scale [10]. The idea that the gluonic components of colliding nucleons dominate in high energy collisions was first presented in Ref. [11]. It was motivated by the fact that the gluon-gluon perturbative cross sections are larger than the quark-antiquark ones. A two-step equilibration of QGP was proposed in [12–14] assuming that the gluon thermalization is accomplished already at the proper time τ_s while the quark-antiquark chemical equilibration proceeds until later times $\tau_{\rm th} > \tau_g$. It was shown in Ref. [2] that $\tau_{\rm th} = 5 \div 10$ fm/c. Such a scenario for high energy A+A collisions was considered by several authors, see, e.g., Refs. [13, 15–24]. The *pure glue* scenario for the initial state in Pb+Pb collisions at Large Hadron Collider (LHC) energies was recently discussed in Refs. [25, 26]. The entropy generation in chemically nonequilibrium QGP has been considered in [27].

In order to highlight possible signatures of the pure glue initial scenario, below we describe the evolution of the QGP created in central A+A collisions using the (2+1)–dimensional boost-invariant hydrodynamics. In our approach the quark-antiquark fugacity is introduced to describe the QGP evolution in the absence of the chemical equilibrium. The main emphasis is put on electromagnetic probes (thermal photons and dileptons), which may carry an important information about the deconfined phase. This problem has been already addressed in the literature, see, e.g., [21–23]. However, the main conclusions about the role of chemically nonequilibrium evolution are still controversial. The new aspects of the present study include constructing the equation of state for chemically nonequilibrium QCD matter which is obtained via an interpolation of the lattice data, the analysis of chemical nonequilibrium effects in the dilepton elliptic flow, and demonstrating the importance of the late

'hadronic' stage for the photon spectra.

The paper is organized as follows. In Sec. II we formulate the hydrodynamical model used in calculations. The equation of state of a chemically nonequilibrium system is constructed by interpolating the lattice results for pure gluon and the (2+1) flavour QCD matter. In Sec. III we give some results concerning the space-time evolution of strongly interacting matter produced in central A+A collisions at LHC energies. Spectra and elliptic flows of direct photons and thermal dileptons are analysed, respectively, in Sec. IV and V. Our conclusions are given in Sec. VI.

II. FORMULATION OF THE MODEL

A. Equations of motion

We use a longitudinally boost-invariant (2+1)–dimensional ideal hydrodynamics to describe the evolution of the net baryon-free matter produced in the high-energy A+A collisions. The equations of the relativistic hydrodynamics can be written as ($\hbar = c = 1$)

$$\frac{\partial T^{\mu\nu}}{\partial x^{\nu}} \;=\; 0 \;, \tag{1}$$

where

$$T^{\mu\nu} \;=\; (\varepsilon + P)\, u^{\mu} u^{\nu} \;-\; P g^{\mu\nu} \tag{2}$$

is the energy-momentum tensor, u^{μ} is the 4-velocity, ε and P are the rest-frame energy density and pressure, respectively, and $g^{\mu\nu}$ is the metric tensor with $g^{00} = 1$. Below we use the light-cone (Milne) coordinates (τ, x, y, η), where $\tau = \sqrt{t^2 - z^2}$ (z is the beam axis) and $\eta = \frac{1}{2} \ln \frac{t+z}{t-z}$, is the space-time rapidity. In the case of the longitudinal boost–invariant (2+1)–dimensional flow one can represent the 4-velocity as [16, 29]

$$u^{\mu} = \gamma_{\perp} (\cosh \eta, \boldsymbol{v}_{\perp}, \sinh \eta)^{\mu}, \tag{3}$$

where $\boldsymbol{v}_{\perp}$ is the transverse velocity in the symmetric plane $z = 0$, and $\gamma_{\perp} = (1 - v_{\perp}^2)^{-1/2}$. To solve Eq. (1) one needs the equation of state (EoS), i.e., the relation connecting P and ε. For chemically nonequilibrium matter considered in this paper, $P = P(\varepsilon, \lambda)$, where λ is the (anti)quark fugacity. In principle, one should also solve additional rate equations, defining the evolution of λ (see, e.g., [15, 16, 23, 28]). In the next section a simple analytic parametrization for λ as a function of the proper time is introduced.

It is useful to introduce the local proper time of a fluid cell element τ_P. Its space-time dependence is determined by the equations

$$u^\mu \partial_\mu \tau_P \;=\; 1 \;, \qquad \tau_P(\tau_0, x, y, \eta) \;=\; \tau_0 \;, \tag{4}$$

where the parameter τ_0 corresponds to initial longitudinal proper time of the hydrodynamic expansion. Equation (4) should be solved simultaneously with Eq. (1). In general, τ_P is less than the 'global' time τ due to a presence of non-zero transverse flow. In a limiting case of the (1+1)–dimensional Bjorken expansion [30], one has $v_\perp = 0$ and $\tau_P = \tau$.

B. Equation of state of chemically nonequilibrium QCD matter

We use the lattice QCD calculations for the EoS of the strongly interacting matter in two limiting cases: 1) the chemically equilibrium QCD matter [32, 33], 2) the SU(3) gluodynamics without (anti)quarks [34, 35]. In the following we denote these cases as FQ (Full QCD) and PG (Pure Glue), respectively. The FQ case corresponds to the (2+1)-flavour QCD calculations which predict the crossover-type transition at $T \sim 155$ MeV. The PG calculation predicts the first-order phase transition at $T = T_c \simeq 270$ MeV. The temperature dependencies of the pressure and energy density for FQ and PG scenarios are represented in Fig. 1. Larger values of P and ε in the FQ calculation appear due to the contribution of quark-antiquark degrees of freedom. Note the discontinuity of $\varepsilon(T)$ at $T = T_c$ in the PG case. Very small values of P and ε at $T < T_c$ in the PG matter originate from large masses of glueballs ($M_g \gg T_c$) representing the confined phase [35].

The suppression of the quark and antiquark densities as compared to their equilibrium values at given temperature is characterized by the (anti)quark fugacity λ (for details, see Ref. [27]). Generalizing the lattice EoS for the chemically nonequilibrium case with $\lambda < 1$ is not a straightforward task. We obtain the P and ε values at fixed T and λ by a linear interpolation (LI) between the the PG and FQ cases[1]:

$$P\,(T, \lambda) \;=\; \lambda\, P_{\rm FQ}(T) + (1-\lambda)\, P_{\rm PG}(T)\,, \tag{5}$$

$$\varepsilon\,(T, \lambda) \;=\; \lambda\, \varepsilon_{\rm FQ}(T) + (1-\lambda)\, \varepsilon_{\rm PG}(T)\,. \tag{6}$$

[1] For brevity, we denote this equation of state as EoS-LI.

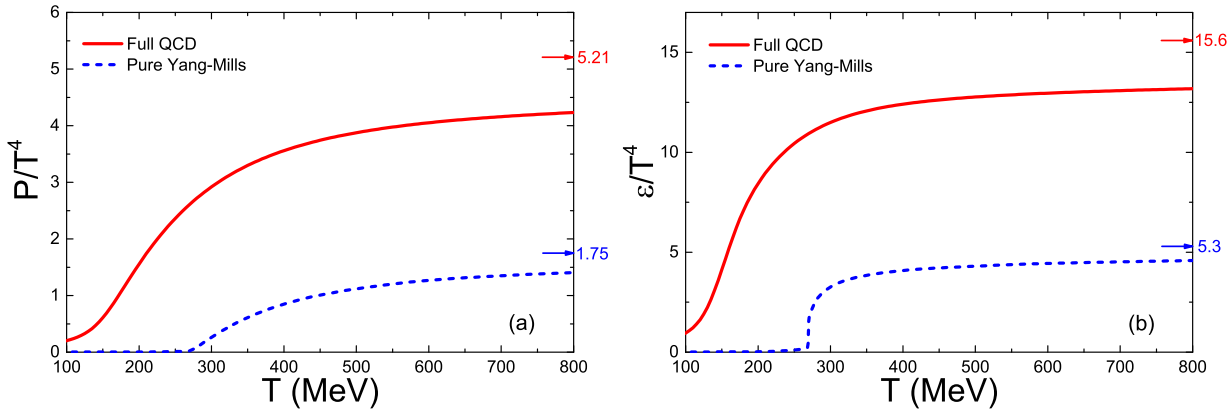

FIG. 1: (Color online) Temperature dependence of the scaled pressure (a) and energy density (b) obtained in lattice QCD calculations of Refs. [32, 35]. The solid and dashed lines correspond to the FQ ($N_f = 2+1$) and PG ($N_f = 0$) cases, respectively. The horizontal arrows indicate the asymptotic (Stefan-Boltzmann) values of P/T^4 and ε/T^4 at large temperatures.

After excluding the temperature variable in Eqs. (5)–(6), one gets the relation $P = P(\varepsilon, \lambda)$ which is used in hydrodynamic simulations. In the limits $\lambda = 0$ and $\lambda = 1$ one gets the thermodynamic functions of the PG and FQ matter, respectively. Note that the linear λ–dependence of P and ε is a characteristic feature of the ideal gas of massless gluons and (anti)quarks studied in Refs. [26, 27].

It is interesting that the ε–dependence of pressure needed for the hydrodynamical calculations appears to be rather similar in PG and FP matter. This is shown in Fig. 2. The pressure values for EoS-LI will change from $P = P_{\rm PG}(\varepsilon)$ at the initial stage of the A+A collision to $P = P_{\rm FQ}(\varepsilon)$ during the later stage of chemical equilibration[2]. As follows from Fig. 2, the both equations of state show almost linear $P(\varepsilon)$ dependence in the considered range, but which is softer than that of the ideal gas of massless partons.

Using Eqs. (5) and (6) and basic thermodynamic identities, one can calculate the total density of (anti)quarks n_q and the entropy density s. The following relations are obtained

$$n_q\,(T,\lambda) \;=\; \frac{\lambda}{T}\,(P_{\rm FQ} - P_{\rm PG}), \tag{7}$$

$$s\,(T,\lambda) \;=\; \lambda\, s_{\rm FQ}(T) + (1-\lambda)\, s_{\rm PG}(T) - n_q(T,\lambda)\ln\lambda\,. \tag{8}$$

The two-dimensional plots of P and ε for the chemically nonequilibrium QGP are shown

[2] Possible supercooling phenomena may change this behavior.

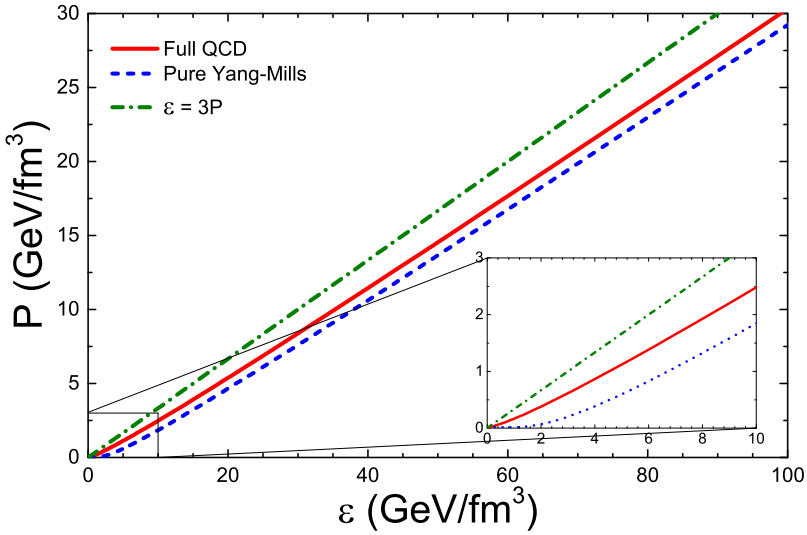

FIG. 2: (Color online) Pressure as a function of energy density in FQ (solid curve) and PG (dashed curve) cases obtained in lattice calculations [32, 35]. Additionally, the $P = \varepsilon/3$ dependence for the ultrarelativistic ideal gas is shown. The inset shows the results at smaller energy densities.

in Fig. 3. The EoS-LI contains the first-order phase transition at $T_c = 270$ MeV. The latent heat of this transition depends on λ, and it goes to zero at $\lambda \to 1$.

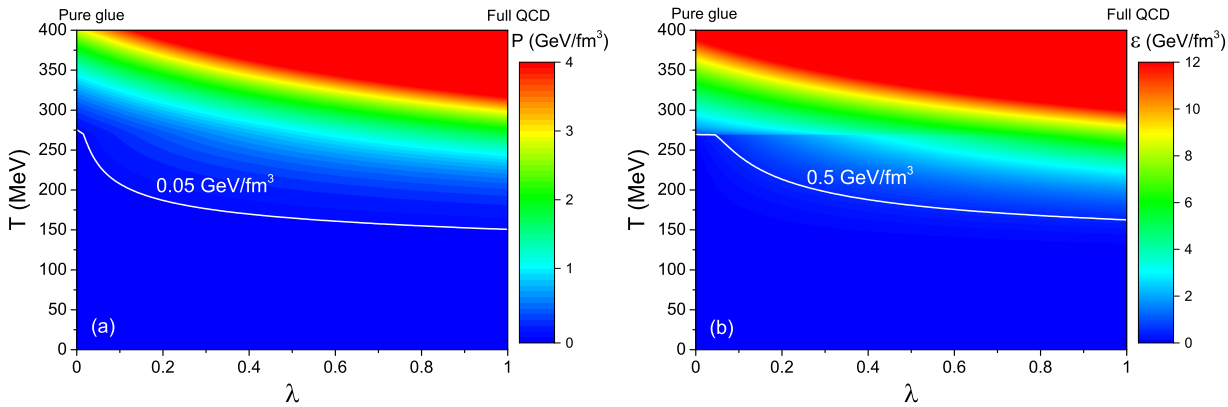

FIG. 3: (Color online) Density plots of pressure (a) and energy density (b) for chemically non-equilibrium QGP calculated from Eqs. (5) and (6). The black solid lines show contours $P = 0.05$ GeV/fm^3 (a) and $\varepsilon = 0.5$ GeV/fm^3 (b).

Below we assume that at $\tau = \tau_0$ the initial (anti)quark densities vanish in all cells and gluons are in thermal and chemical equilibrium. Similarly to Refs. [26, 27] we postulate that λ is an explicit function of the local proper time τ_P which increases from $\lambda = 0$ at $\tau_P = \tau_0$

to $\lambda = 1$ at $\tau_P - \tau_0 \to \infty$. The following parametrization is used:

$$\lambda(\tau_P) = 1 - \exp\left(\frac{\tau_0 - \tau_P}{\tau_*}\right), \tag{9}$$

where τ_* is the model parameter characterizing the quark chemical equilibration time. There are different estimates for τ_* in the literature ranging from $\tau_* \sim 1$ fm/c [31] to $\tau_* \sim 5$ fm/c [2]. Note that $\tau_* = 0$ corresponds to the instantaneous chemical equilibration of quarks and gluons.

C. Initial conditions

We consider Pb+Pb collisions at the LHC with the c.m. energy per nucleon pair $\sqrt{s_{NN}} = 2.76$ TeV. In our calculations we choose $\tau_0 = 0.1$ fm/c as the initial time of the hydrodynamic evolution. It is assumed that there is no initial transverse flow, i.e., $\boldsymbol{v}_\perp(\tau_0, x, y) = 0$, and the initial energy density profile is proportional to the linear combination of the transverse distributions of wounded nucleons and binary collisions taken from the event-averaged Monte Carlo Glauber model as suggested in the GLISSANDO code [36]. The coefficient of proportionality in the initial ε-profile is fixed to reproduce the observed hadronic spectra within the *chemically equilibrium* simulation with the full QCD EoS for a given centrality interval (see Ref. [37] for details). We use the same initial energy density profile in our calculations for the chemically nonequilibrium case.

III. NUMERICAL RESULTS OF HYDRODYNAMIC SIMULATIONS

Equations (1) and (4) are solved using the (2+1)–dimensional version of the vHLLE hydro code [38]. The EoS tables $P = P(\varepsilon, \lambda)$ for hydrodynamic simulations were prepared as described in Sec. II B. We consider the 0–20% and 20–40% central Pb+Pb collisions.

The density plot of the quark fugacity λ in the $x-\tau$ plane is shown in Fig. 4a. The dashed line shows the isotherm $T = 155$ MeV which presumably corresponds to the hadronization hypersurface. One can see that typical lifetimes of the deconfined phase in the considered reaction do not exceed 10 fm/c. From Fig. 4a one observes that deviations from chemical equilibrium ($\lambda \lesssim 0.9$) survive up to the hadronization stage. As discussed in Ref. [27] this may lead to the suppression of(anti)baryon-to-pion ratios observed [39] for the considered reaction.

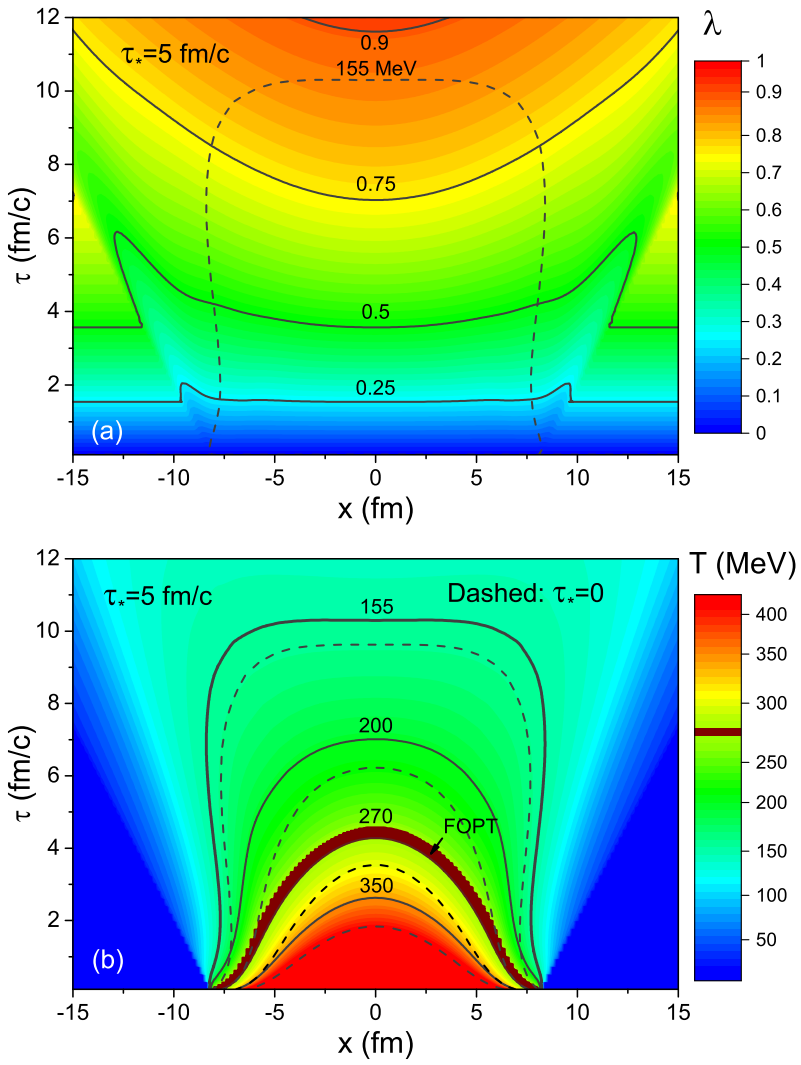

FIG. 4: (Color online) Density plots of the quark fugacity (a) and temperature (b) in the $x-\tau$ plane for the 0–20% most central Pb+Pb collisions at $\sqrt{s_{NN}} = 2.76$ TeV. The solid lines show contours of λ and T (in MeV). The dashed line in (a) corresponds to the isotherm $T = 155$ MeV. The dark region labeled by FOPT corresponds to the mixed-phase region of the first-order phase transition at $T = T_c \simeq$ 270 MeV. The dashed lines in (b) are isotherms calculated for equilibrium matter with $\lambda = 1$.

Figure 4b shows the color plot of the temperature in the coordinates (x, τ). The solid and dashed lines correspond to $\tau_* = 5$ fm/c and $\tau_* = 0$, respectively. One can see that the chemically undersaturated matter is hotter as compared to the equilibrium case ($\lambda =$

1)[3]. This is a consequence of reduced number of degrees of freedom in such a matter. According to Fig. 4b, typical lifetimes of the mixed phase are rather short, they do not exceed 0.5 fm/c. This is at variance with calculations in the (1+1) dimensional hydrodynamics which predict [40] much larger lifetimes of the mixed phase within the chemically equilibrated bag model.

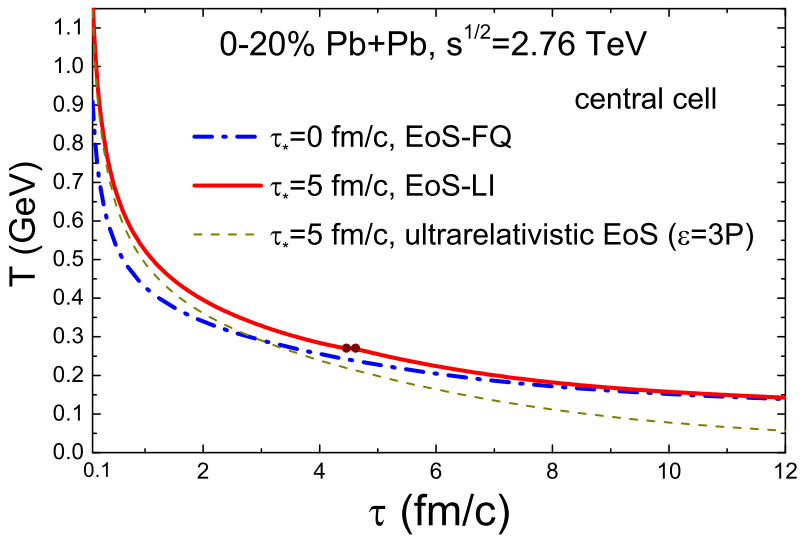

FIG. 5: (Color online) Temperature in the central cell as a function of proper time for the 0–20% central Pb+Pb collisions at $\sqrt{s_{NN}} = 2.76$ TeV. The dashed and solid lines are calculated for $\tau_* = 0$ and $\tau_* = 5$ fm/c, respectively. Points between filled dots on the solid curve correspond to mixed-phase states of deconfinement phase transition. The dash-dotted line is calculated for $\tau_* = 5$ fm/c assuming the ideal gas EoS.

Figure 5 shows the evolution of temperature in the central cell ($\boldsymbol{r} = 0$) for $\tau_* = 0$ and $\tau_* = 5$ fm/c. In the second case we compare the calculations for EoS-LI (the solid line) and for the ideal gas of massless partons [27] (the dash-dotted line).

Chemical nonequilibrium effects lead to the total entropy growth. This was shown in Ref. [27] within the Bjorken longitudinal hydrodynamics. We present here a similar analysis in the (2+1)–dimensional model. The following expression for the total entropy S can be written within the ideal hydrodynamics [40]:

$$S = \int d\sigma^\mu u_\mu s \,, \tag{10}$$

[3] Note that in both cases we take the same profile of the energy density at $\tau = \tau_0$.

where s is the entropy density and $d\sigma^\mu$ is the element of a space-time hypersurface which we choose below[4] as the surface of constant proper time τ. Using Eq. (3), one can show that $d\sigma^\mu u_\mu = \gamma_\perp \tau d^2x_\perp d\eta$ for such a hypersurface. Substituting this relation into Eq. (10) leads to the following equation for the total entropy per unit space-time rapidity in the (2+1)–dimensional hydrodynamics

$$\frac{dS(\tau)}{d\eta} = \tau \int d^2x_\perp \gamma_\perp(\tau, \boldsymbol{x}_\perp) s(\tau, \boldsymbol{x}_\perp) \,. \tag{11}$$

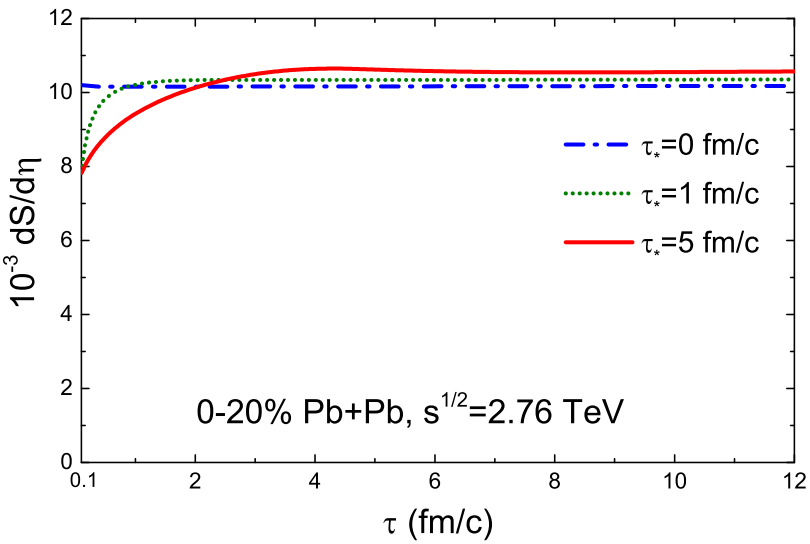

FIG. 6: (Color online) Total entropy per unit space-time rapidity as a function of proper time τ for the 0–20% central Pb+Pb collisions at $\sqrt{s_{NN}} = 2.76$ TeV. The dashed, dotted and solid lines correspond to the parameters $\tau_* = 0, 1$ and 5 fm/c, respectively.

The results of the entropy calculations for the 0–20% central Pb+Pb collisions are shown in Fig. 6. At $\tau_* = 5$ fm/c the relative increase of the entropy is about 30%. Approximately the same relative increase has been obtained [27] in the (1+1)–dimensional calculation for the ideal gas EoS. Note, that more consistent calculations for nonzero τ_* would require renormalizing the initial energy density profiles to get the same final pion multiplicities as in the equilibrium case. The asymptotic values of $dS/d\eta$ for different choices of τ_* in Fig. 6 will be then the same.

[4] In the case of chemical equilibrium S is constant and does not depend on the choice of a hypersurface.

IV. DIRECT PHOTON EMISSION

The emission of direct[5] photons from expanding matter created in relativistic A+A collisions has several components [41, 42]: a) 'thermal' photons from the high-temperature deconfined phase, b) direct photons from the low-temperature hadronic phase, c) 'prompt' photons from binary collisions of initial nucleons. The contribution of prompt photons becomes dominant at large transverse momenta. As we will see below, this greatly reduces the sensitivity of photon p_T-spectra to chemical nonequilibrium effects. However, the situation with transverse flows of photons is different because of low azimuthal anisotropy of prompt photons. Note that the ALICE experiments reveal [43] large elliptic flows of direct photons, which still can not be explained in the chemically equilibrium scenario [41].

Within the leading order approximation in the strong coupling constant, the following sources of thermal photon production in the deconfined matter are dominant [44]:
1) the QCD Compton scattering ($X + g \to X + \gamma$, where $X = q, \overline{q}$),
2) the quark-antiquark annihilation ($q + \overline{q} \to g + \gamma$),
3) the bremsstrahlung reactions ($X + Y \to X + Y + \gamma$, where $X = q, \overline{q}$ and $Y = q, \overline{q}, g$),
4) the 'off-shell' $q\overline{q}$–annihilation with rescatterings of (anti)quark on another parton in the initial state[6]. It is clear that photons can not be produced in a pure glue matter without charged (anti)quark partons.

Let us consider the invariant photon production rate (PPR) in the chemically undersaturated quark-gluon plasma (uQGP) with the temperature T and the quark fugacity λ. Below we denote this quantity as $\Gamma(\widetilde{E}, T, \lambda)$, where $\widetilde{E}$ is the photon energy in the rest frame of the fluid element. The limiting case of complete chemical equilibrium ($\lambda = 1$) is considered in Appendix A. We use the analytic parametrization for $\Gamma(\widetilde{E}, T) = \Gamma(\widetilde{E}, T, 1)$ suggested in Ref. [44]. Equations (A1)–(A2) give the explicit expressions for $\Gamma_i(\widetilde{E}, T)$, which are the PPR of processes $i = 1, 2$ in the chemically equilibrium QGP.

To calculate PPR for arbitrary λ we introduce the additional suppression factor λ for each quark and antiquark [26, 27] in initial states of the processes 1-4. In particular, the

[5] By direct photons we denote the 'non-cocktail' photons i.e. those which are not produced in decays of $\pi^0, \eta, \rho, \eta', \phi$ mesons in the final stage of the reaction.
[6] According to Ref. [45], the next-to-leading order corrections to the rate of photon production in equilibrium QGP do not exceed 20%.

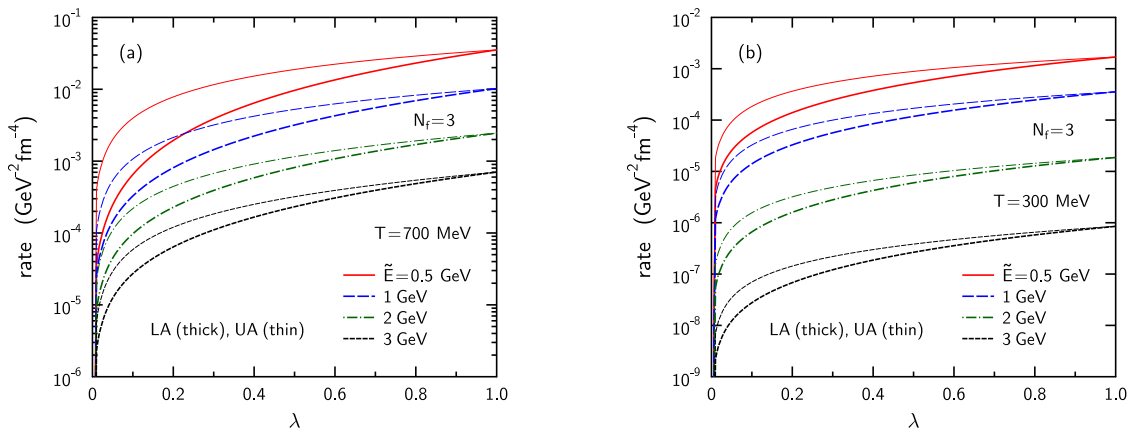

FIG. 7: (Color online) Thermal photon production rates in uQGP as functions of quark fugacity λ at temperatures $T = 700$ (a) and 300 (b) MeV for different values of rest-frame photon energy $\widetilde{E}$. Thick and thin lines are calculated by using Eq. (12) and (13), respectively.

rates of the processes 1 and 2 will be suppressed by the factors λ and λ^2, respectively. Analogous procedure for the processes 3-4 is not trivial, as the contribution of partons $Y = g$ is not suppressed as compared to $Y = q, \overline{q}$. Similar to Ref. [22], we apply two different approximations for $\Gamma(\widetilde{E}, T, \lambda)$:

$$\text{LA:} \qquad \Gamma(\widetilde{E}, T, \lambda) = \lambda \Gamma_1(\widetilde{E}, T) + \lambda^2 \left[\Gamma(\widetilde{E}, T) - \Gamma_1(\widetilde{E}, T) \right], \tag{12}$$

$$\text{UA:} \qquad \Gamma(\widetilde{E}, T, \lambda) = \lambda^2 \Gamma_2(\widetilde{E}, T) + \lambda \left[\Gamma(\widetilde{E}, T) - \Gamma_2(\widetilde{E}, T) \right], \tag{13}$$

where $\Gamma(\widetilde{E}, T)$ is calculated by using Eqs. (A4)–(A7). It is clear that the approximation LA (UA) underestimates (overestimates) the 'exact' photon production rate in uQGP. The results of PPR calculations using Eqs. (12)–(13) are shown in Fig. 7 for several values of $\widetilde{E}$ and T. One can see that the difference between the parametrizations LA and UA increases with T. Note that large temperatures correspond to early stages of a heavy–ion collision. At these stages λ are rather small in the pure glue initial scenario [26].

In our case of a boost invariant (2+1)–dimensional expansion the invariant yield of thermal photons is calculated as

$$\frac{dN_\gamma^{\rm th}}{d^2 p_T dY} = \int d^2 x_T \int_{\tau_0}^{+\infty} d\tau\, \tau \int_{-\infty}^{+\infty} d\eta\, \Gamma(\widetilde{E}, T, \lambda)\, \theta(T - T_f)\,, \tag{14}$$

where p_T is the transverse momentum of the photon, Y is its longitudinal rapidity, $\widetilde{E} = \gamma_\perp p_T \left[\cosh(Y - \eta) - v_x \cos\varphi - v_y \sin\varphi \right]$ (φ is the angle between $\boldsymbol{p}_T$ and the reac-

tion plane), $\theta(x) = \left[1 + \mathrm{sgn}(x)\right]/2$, and T_f is the cutoff parameter determining the minimal temperature.

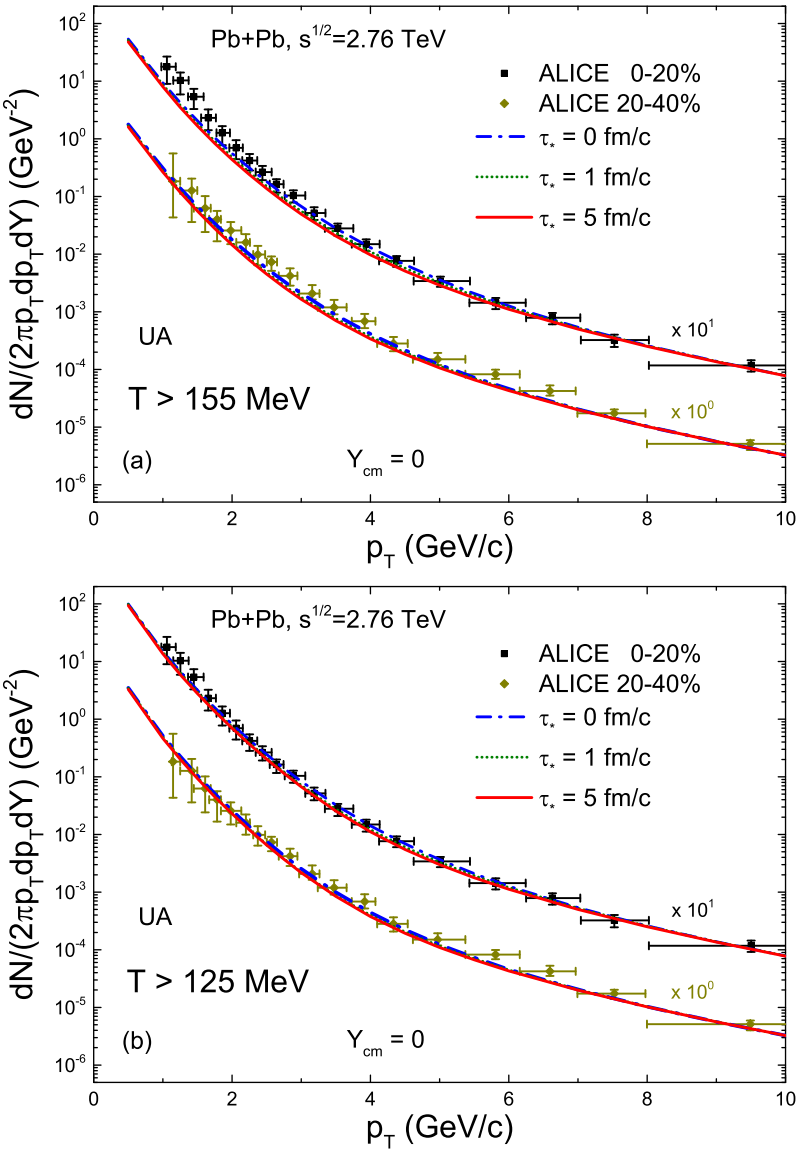

FIG. 8: (Color online) Spectra of direct photons in the 0–20% central Pb+Pb collisions at $\sqrt{s_{NN}} = 2.76$ TeV calculated using Eqs. (13)–(14) with the cutoff temperatures $T_f = 155$ (a) and 125 (b) MeV. The dash-dotted, dotted and solid lines correspond to $\tau_* = 0, 1$ and 5 fm/c, respectively. Dots with error bars show experimental data [46].

As mentioned above, spectra of direct photons include, in addition to the thermal component, also the contribution of prompt photons from collision of nucleons in cold initial nuclei. The second contribution is normally found by using the perturbative QCD calculations of

photon production in a single pp-collision at the same $\sqrt{s_{NN}}$. The obtained photon yield is scaled by the average number of nucleon collisions for a given centrality class. Below we use the prompt photon spectra in central Pb+Pb collisions at LHC reported in Refs. [43, 46]. According to our calculations, the contribution of prompt photons in such reactions becomes dominant at high transverse momenta $p_T \gtrsim 5$ GeV/c. Unfortunately, this greatly reduces the sensitivity of combined p_T–spectra of thermal and prompt photons to the EoS and to parameters of chemical nonequilibrium.

Figures 8a, b show the results for the direct photon spectrum in the 0–20% central Pb+Pb collisions at $\sqrt{s_{NN}} = 2.76$ TeV. We have checked that the LA-parametrization of thermal photon emission, Eq. (12), gives only several percent lower yields as compared to the alternative UA-choice. Therefore, we present here only the results based on Eq. (13). To estimate contributions of thermal photon emission from late stages of the reaction, we perform calculations for two choices of the cut-off temperature, $T_f = 155$ and 125 MeV[7]. Comparison of Figs. 8a and b shows that thermal photon emission from the low-temperature ('hadronic') stage $T \lesssim 155$ MeV gives only a slight change of the yield at intermediate $p_T = 2 \div 6$ GeV/c. On the other hand, such emission noticeably increases the photon yield at $p_T \lesssim 2$ GeV/c. Including this additional source of thermal photons leads to a better agreement with observed data.

The direct photon production in Pb+Pb collisions at LHC has been considered in various theoretical models which include relativistic ideal [47, 48] or viscous [41] hydrodynamics, and the PHSD off-shell transport approach [49]. These studies describe experimental p_T-spectra of photons with a similar quality. Thus, as noted in Ref. [46], the present uncertainties in the ALICE photon data do not allow to discriminate between various models and scenarios.

The photon elliptic flow $v_2^\gamma(p_T)$ is calculated as

$$v_2^\gamma(p_T) = \frac{\int_0^{2\pi} d\varphi \, \frac{dN_\gamma}{d^2p_T dY} \, \cos(2\varphi)}{\int_0^{2\pi} d\varphi \, \frac{dN_\gamma}{d^2p_T dY}} \, . \tag{15}$$

The photon spectrum, entering this equation includes both thermal and prompt components. We assume that prompt photons are azimuthally symmetric. Therefore, they contribute only

[7] In principle, the photon production in hadronic phase at temperatures $T \lesssim 155$ MeV may proceed with different emission rates as compared to the deconfined phase. However, as demonstrated in [41, 50], one can safely use the same rates for the photon emission also below the hadronization temperature. Note, that this approximation may not be valid for baryon-rich matter.

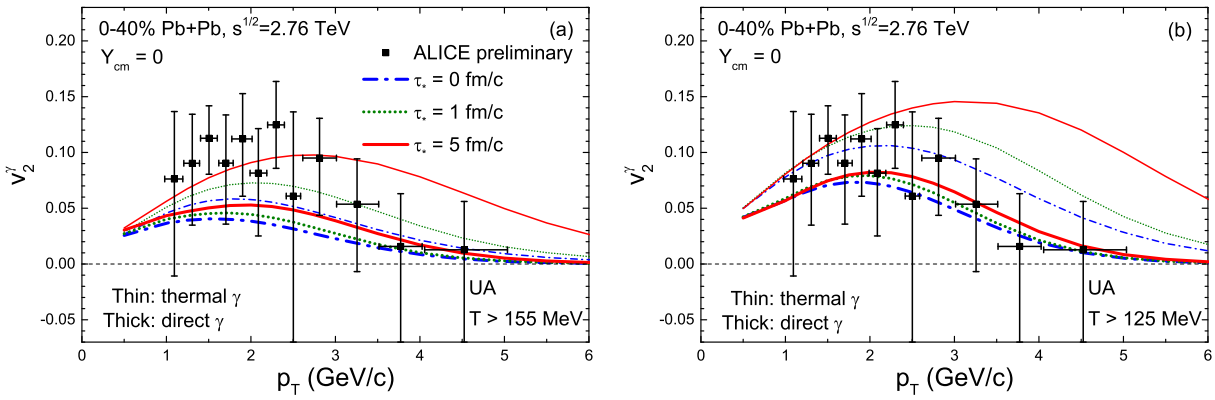

FIG. 9: (Color online) Elliptic flow of direct photons as a function of transverse momentum in the $0-40\%$ central Pb+Pb collisions at $\sqrt{s_{NN}} = 2.76$ TeV calculated with the cutoff temperatures $T_f = 155$ (a) and 125 (b) MeV. The dash-dotted, dotted and solid lines correspond to $\tau_* = 0, 1$ and 5 fm/c, respectively. Thick (thin) curves are calculated with (without) the contribution of prompt photons in Eq. (15). Data are taken from Ref. [43].

to the denominator of Eq. (15) reducing v_2^γ at large p_T.

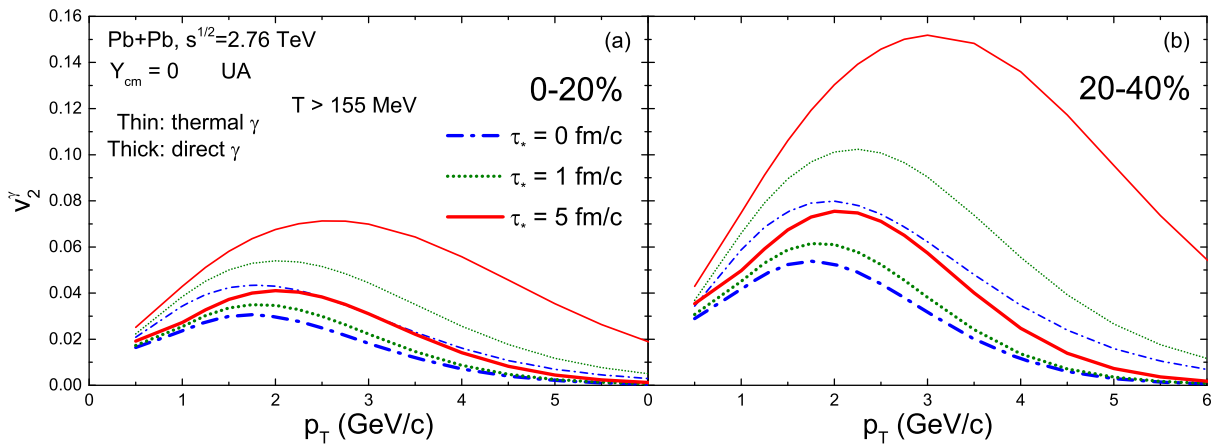

FIG. 10: (Color online) Elliptic flow of the direct (thick lines) and thermal (thin lines) photons for the 0–20% (a) and 20–40% (b) central Pb+Pb collisions at $\sqrt{s_{\rm NN}} = 2.76$ TeV.

The results for direct photon elliptic flow in the 0–40% central Pb+Pb collisions at $\sqrt{s_{NN}} = 2.76$ TeV are shown in Figs. 9 a, b. One can see that the initial undersaturation of quarks leads to a noticeable enhancement of v_2^γ. The comparison of thick and thin lines

shows that this enhancement is significantly reduced due to the presence of prompt photons[8]. An interesting conclusion comes from the analysis of different cutoff temperatures. One can see that adding the contribution of a colder 'hadronic' stage increases the photon elliptic flow by a factor of about two. This leads to a much better agreement with the ALICE data. The latter are noticeably underestimated in the chemically equilibrium scenario ($\tau_* = 0$). The physical reason for the v_2 increase for lower T_f is rather clear. It is explained by the increase of collective flow velocities at later times. Despite of the fact that less quarks are produced at late stages, their elliptic flow will be stronger.

To study possible influence of the centrality choice, in Fig. 10 we calculate the photon elliptic flows for the same reaction, but taking more narrow centrality classes, 0–20% and 20–40%. One can see, that the photon elliptic flow and its sensitivity to chemical nonequilibrium effects becomes stronger for larger impact parameters. This behavior is explained by increased eccentricities of quark fireballs in less central events.

V. THERMAL DILEPTON EMISSION

The rate of thermal dilepton production from the lowest-order quark-antiquark annihilation processes $q\overline{q} \to e^+e^-$ in the net baryon-free uQGP can be written as[9]:

$$\frac{dN}{d^4x\, d^4Q} = C_q\, \lambda^2 \exp\left(-\frac{Qu}{T}\right), \tag{16}$$

where $Q = p_+ + p_-$ is the dilepton total 4-momentum, T and u are, respectively, the local values of temperature and 4-velocity of QGP. The coefficient $C_q = \frac{\alpha^2}{4\pi^4} F_q$, where α and F_q are defined in Eq. (A1). Note that Eq. (16) is written in the Boltzmann approximation for the (anti)quark phase-space distributions and assumes that all quarks and leptons are massless. The λ^2 factor in Eq. (16) takes into account the (anti)quark suppression in the chemically nonequilibrium QGP.

Introducing the dilepton invariant mass $M = \sqrt{Q^2}$, one has

$$Q^\mu = (M_\perp \cosh Y, \boldsymbol{Q}_\perp, M_\perp \sinh Y)\ , \tag{17}$$

[8] Similar conclusions have been made in Refs. [22, 23].

[9] An analogous expression in the limit of chemically equilibrated plasma ($\lambda = 1$) has been suggested in [29]. First calculations of the dilepton emission in uQGP have been made in Refs. [17, 28].

where $M_\perp = \sqrt{M^2 + \boldsymbol{Q}_\perp^2}$, and $Y = \tanh^{-1}(Q_z/Q_0)$ is the longitudinal rapidity of the lepton pair. Using Eq. (3) for the collective 4-velocity in the (2+1)–dimensional hydrodynamics, one gets the expression for the rest-frame dilepton's total energy

$$(Qu) = \gamma_\perp \left[M_\perp \cosh(Y - \eta) - \boldsymbol{Q}_\perp \boldsymbol{v}_\perp \right]. \tag{18}$$

Let us denote by φ and φ_u the angles of $\boldsymbol{Q}_\perp$ and $\boldsymbol{v}_\perp$ with respect to the x-axis, respectively. Then one can substitute $\boldsymbol{Q}_\perp \boldsymbol{v}_\perp = Q_\perp v_\perp \cos(\varphi - \varphi_u)$ in the r.h.s. of Eq. (18).

From Eq. (16), using the relations $d^4x = \tau d\tau\, d^2x_\perp d\eta$ and $d^4Q = M dM dY d^2Q_\perp$, after integrating over the space–time rapidity η, we obtain:

$$\frac{dN}{dM^2 dY d\varphi} = C_q \int d^2x_\perp \int\limits_{\tau_0}^{+\infty} d\tau\, \tau\, \lambda^2(\tau, \boldsymbol{x}_\perp)\, J(M, \tau, \boldsymbol{x}_\perp)\, \theta(T - T_f)\,, \tag{19}$$

where

$$J(M, \tau, \boldsymbol{x}_\perp) = \int\limits_0^\infty dQ_\perp Q_\perp K_0 \left(\frac{\gamma_\perp M_\perp}{T} \right) \exp\left(\frac{\gamma_\perp \boldsymbol{Q}_\perp \boldsymbol{v}_\perp}{T} \right). \tag{20}$$

Hereinafter we denote by $K_\nu(x)$ and $I_\nu(x)$ the modified Bessel functions of the order ν. One can see that the dilepton spectrum (19) does not depend on Y within the (2+1)–dimensional hydrodynamics.

Explicit relations for the invariant mass distribution and the elliptic flow of thermal dileptons, obtained from (19)–(20), are given in Eqs. (B1)–(B4) of Appendix B. It is interesting that the dilepton mass spectrum does not depend explicitly on the transverse collective velocity $\boldsymbol{v}_\perp$ (see (B1), (B3)). This is at variance with the p_T-spectra of thermal photons which are defined by a superposition of exponents $\exp(-p_T/T_{\rm eff})$, where $T_{\rm eff}$ is the "blue-shifted" effective temperature $T_{\rm eff} = T\sqrt{(1+v_\perp)/(1-v_\perp)}$.

In the limiting case of (1+1)–dimensional hydrodynamics one gets for purely central collisions [26]

$$\frac{dN}{dM^2 dY} \simeq 2\pi^2 R^2 C_q M \int\limits_{\tau_0}^{\tau_f} d\tau\, \tau\, T(\tau)\, K_1\left[\frac{M}{T(\tau)} \right] \lambda^2(\tau) \qquad (v_\perp = 0)\,, \tag{21}$$

where R is the geometrical radius of colliding nuclei and τ_f is determined from $T(\tau_f) = T_f$.

The results of calculating the dilepton mass spectrum in central Pb+Pb collisions at $\sqrt{s_{NN}} = 2.76$ TeV are shown in Fig. 11 for the cut-off temperature $T_f = 155$ MeV. One

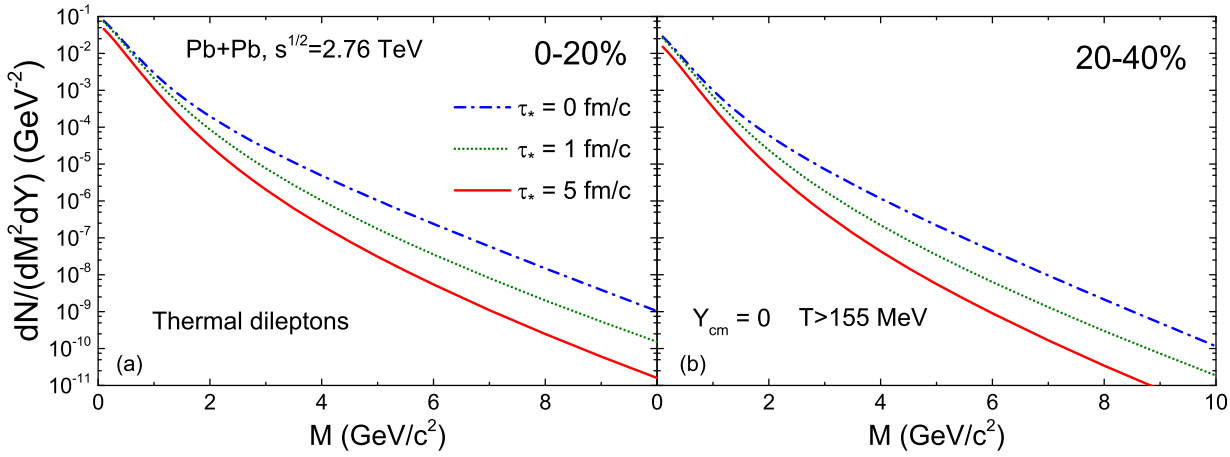

FIG. 11: (Color online) Invariant mass distribution of thermal dileptons in the 0–20% (a) and 20–40% (b) central Pb+Pb collisions at $\sqrt{s_{NN}} = 2.76$ TeV calculated for $\tau_* = 0, 1$ and 5 fm/c. All results correspond to the cut-off temperature $T_f = 155$ MeV.

can see that the initial quark suppression leads to a strong reduction of the dilepton yield at $M \gtrsim 2$ GeV. Note that we do not add contributions of hard (Drell-Yan) dileptons [42] produced in binary collisions of initial nucleons.

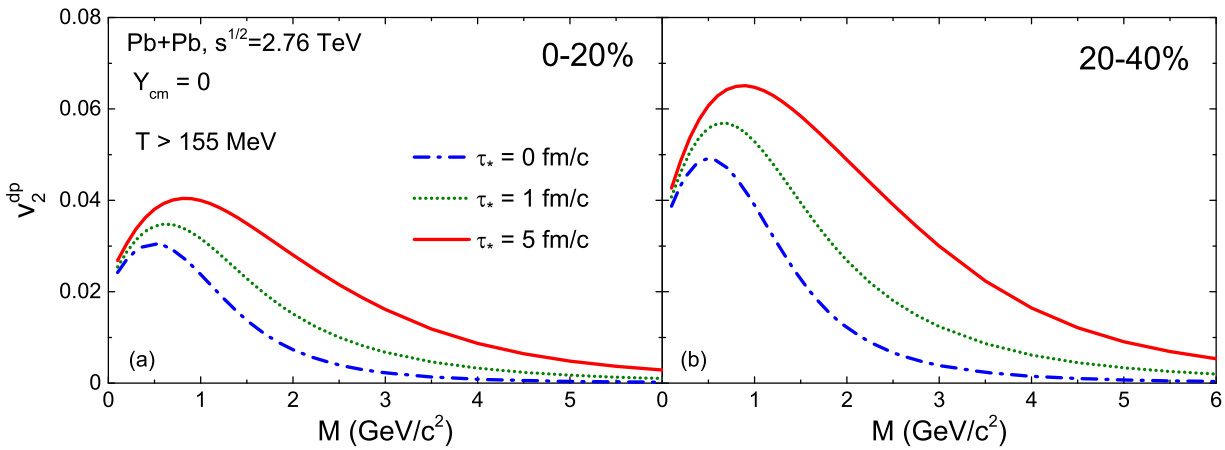

FIG. 12: (Color online) Same as Fig. 11 but for elliptic flow of thermal dileptons.

As shown in Appendix B, the elliptic flow of thermal dileptons strongly depends both on the direction and magnitude of the transverse collective velocity. Note, that the previous analysis of dilepton elliptic flow of Refs. [52, 53] corresponds to the limit of complete chemical equilibrium ($\lambda = 1$).

The elliptic flows of thermal dileptons in the same reaction, calculated in accordance

with Eq. (B2), are shown in Fig. 12 for several values of τ_*. Similar to direct photons we predict a strong enhancement of the dilepton elliptic flow as compared to the equilibrium scenario ($\tau_* = 0$). Note that $v_2^{\rm dp}$–values are larger for more peripheral events.

VI. CONCLUSIONS

In this paper we presented the detailed calculations of the electromagnetic observables in Pb+Pb collisions at the LHC energy for different assumptions about the initial state of produced partonic matter. In our calculations we have used a rather advanced hydrodynamic model which was previously used to describe hadronic observables. Inclusion of the photon emission at late hadronic stages leads to a better agreement with the ALICE data for direct photons.

In the non-equilibrium scenario the thermal production of the high-p_T photons is significantly suppressed compared to the equilibrium case. However, since the high-p_T photon production is dominated by the prompt photons from initial parton scatterings, we do not find a strong suppression of the total direct photon spectra. Our analysis shows that the p_T-spectra of such photons calculated for equilibrium and nonequilibrium scenarios differ at most by a factor of two and these differences are within the error bars of experimental data. Much stronger effects are found for the thermal dilepton spectra, especially at large invariant masses $M \gtrsim 2$ GeV, where the deviations between two scenarios reach one-two orders of magnitude. Unfortunately, the corresponding experimental data is not available yet.

Our hydrodynamic approach has also allowed us to calculate the elliptic flow parameter v_2, which characterizes the azimuthal anisotropy of the direct photon and dilepton emission. We have found a rather significant enhancement of the v_2 for the pure glue initial state for both photons and dileptons. However, the available experimental data for photons are not accurate enough to discriminate between the considered scenarios for the initial stage. We hope that this will be possible in the future.

Acknowledgments

The authors thank E.L. Bratkovskaya for useful discussions. This work was partially supported by the Helmholtz International Center for FAIR, Germany, and by the Program of Fundamental Research of the Department of Physics and Astronomy of National Academy of Sciences of Ukraine. L.M.S. and I.N.M. acknowledge a partial support from the grant NSH-932.2014.2 of the Russian Ministry of Education and Science.

APPENDIX A: PHOTON EMISSION

In this section we consider the PPR in the chemically equilibrium QGP. The processes 1-2 (see Sec. IV) have been analyzed in Ref. [50]. The infrared divergencies of photon production cross sections were regularized by using the hard thermal loop resummation procedure [54]. The following expressions for invariant rates of photon production have been obtained in the lowest order approximation in the strong coupling constant α_S:

$$\Gamma_i(\widetilde{E},T) \equiv E\frac{dN_i}{d^3pd^4x} = A_i F_q \alpha\alpha_S T^2 e^{-x} \ln\frac{B_i x}{\alpha_s} \quad (i=1,2)\,. \tag{A1}$$

Here $p^\mu = (E,\boldsymbol{p})^\mu$ is the photon 4-momentum, $\widetilde{E} = p_\mu u^\mu$ is the rest-frame photon energy, $\alpha = e^2 \simeq 1/137$ is the electromagnetic coupling constant, $F_q = \sum_f \left(\frac{e_f}{e}\right)^2$ (e_f is the charge of quarks with flavor f), and $x = \widetilde{E}/T$. Numerical values of constants A_i, B_i are given by the relations

$$A_2 = 2A_1 = \frac{1}{3\pi^2}, \quad B_1 \simeq 1.00, \quad B_2 \simeq 0.112. \tag{A2}$$

In the following we assume that the number of quark flavours $N_f = 3$ and take into account the temperature dependence of α_S by using the parametrization [55]

$$\alpha_S = \frac{6\pi}{(33-2N_f)\ln(8T/T_*)}\,, \tag{A3}$$

where $T_* = 170$ MeV.

The processes 3-4 correspond to higher orders in α_S. The detailed calculations [44] give the following result for the total PPR:

$$\Gamma(\widetilde{E},T) = \sum_{i=1}^{4}\Gamma_i(\widetilde{E},T) = \frac{1}{\pi^2}F_q\alpha\alpha_S T^2\Phi(x)\,, \tag{A4}$$

$$\Phi(x) = (e^x+1)^{-1}\left[\frac{1}{2}\ln\frac{3x}{2\pi\alpha_S} + C_{12}(x) + C_{34}(x)\right], \tag{A5}$$

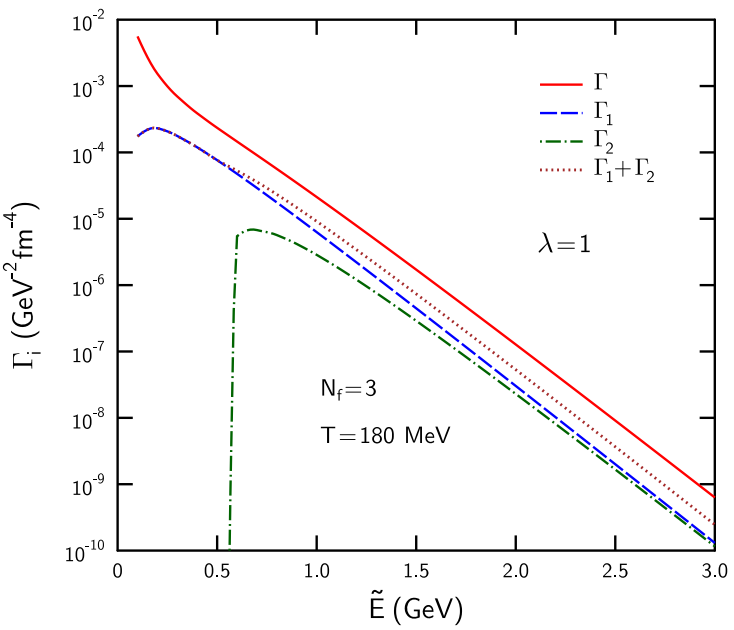

FIG. 13: (Color online) Thermal photon production rates in equilibrium QGP as functions of the rest-frame photon energy at temperature $T = 180$ MeV.

where

$$C_{12}(x) = 0.041\,x^{-1} - 0.3615 + 1.01\,e^{-1.35\,x}, \tag{A6}$$

and

$$C_{34}(x) = \sqrt{1 + \frac{N_f}{6}} \left[\frac{0.548}{x^{3/2}} \ln\left(12.28 + x^{-1}\right) + \frac{0.133\,x}{\sqrt{1 + x/16.27}} \right]. \tag{A7}$$

These formulas become not accurate outside the domain $0.2 \lesssim x \lesssim 50$. Figure 13 shows numerical values of $\Gamma_1, \Gamma_2, \Gamma$ for $T = 180$ MeV. One can see that contributions of processes 3-4 are rather significant at all considered photon energies.

APPENDIX B: DILEPTON EMISSION

The invariant mass spectrum dN/dM^2dY and the elliptic flow $v_2 = v_2(M)$ of thermal dileptons are determined by integrating Eq. (19) over φ with the weights 1 and $\cos(2\varphi)$,

respectively. We get the relations

$$\frac{dN}{dM^2dY} = C_q \int d^2x_\perp \int\limits_{\tau_0}^{+\infty} d\tau\tau\lambda^2(\tau,\boldsymbol{x}_\perp)\, J_1(M,\tau,\boldsymbol{x}_\perp)\,\theta(T-T_f), \tag{B1}$$

$$v_2\frac{dN}{dM^2dY} = C_q \int d^2x_\perp \int\limits_{\tau_0}^{+\infty} d\tau\tau\lambda^2(\tau,\boldsymbol{x}_\perp)\, J_2(M,\tau,\boldsymbol{x}_\perp)\,\theta(T-T_f), \tag{B2}$$

where

$$J_1 = \int\limits_0^{2\pi} d\varphi\, J = 2\pi \int\limits_0^{\infty} dQ_\perp Q_\perp K_0\left(\frac{\gamma_\perp M_\perp}{T}\right) I_0\left(\frac{\gamma_\perp v_\perp Q_\perp}{T}\right) = 2\pi M T K_1\left(\frac{M}{T}\right) \tag{B3}$$

and

$$\begin{aligned} J_2 = \int\limits_0^{2\pi} d\varphi\, J\cos(2\varphi) &= 2\pi\cos(2\varphi_u)\int\limits_0^{\infty} dQ_\perp Q_\perp K_0\left(\frac{\gamma_\perp M_\perp}{T}\right) I_2\left(\frac{\gamma_\perp v_\perp Q_\perp}{T}\right) \\ &= \cos(2\varphi_u)\left\{J_1 - \frac{4\pi T^2}{\gamma_\perp^2-1}\left[K_0\left(\frac{M}{T}\right) - K_0\left(\frac{\gamma_\perp M}{T}\right)\right]\right\}. \end{aligned} \tag{B4}$$

To calculate integrals over $Q_\perp$ in Eqs. (B3)–(B4), we have applied the procedure suggested in [56]. We start from the integral representation

$$K_\nu(x) = x^\nu \int\limits_0^{\infty} \frac{dt}{t^{\nu+1}} \exp\left[-\frac{1}{2}\left(t+\frac{x^2}{t}\right)\right], \tag{B5}$$

and then use the formulae

$$\int\limits_0^{\infty} dQ_\perp Q_\perp e^{-AQ_\perp^2} I_0(BQ_\perp) = \frac{1}{2A}\exp\left(\frac{B^2}{4A}\right), \tag{B6}$$

$$\int\limits_0^{\infty} dQ_\perp Q_\perp e^{-AQ_\perp^2} I_2(BQ_\perp) = \left(\frac{1}{2A} - \frac{2}{B^2}\right)\exp\left(\frac{B^2}{4A}\right) + \frac{2}{B^2}. \tag{B7}$$

The second equation is obtained by using the relation $I_2(x) = I_0(x) - 2I_0'(x)/x$.

Note, that $\cos(2\varphi_u) = (v_x^2 - v_y^2)/v_\perp^2$ in Eq. (B4). It is easy to show that at small $v_\perp$ one gets the approximate relation

$$J_2 \simeq \frac{\pi}{2}\,(v_x^2 - v_y^2)\, M^2 K_2\left(\frac{M}{T}\right) \qquad (v_\perp \ll 1). \tag{B8}$$

Presumably, this limiting case corresponds to early stages of the QGP evolution.

[1] X.-N. Wang, M. Gyulassy, Phys. Rev. D **44**, 3501 (1991).

[2] Z. Xu and C. Greiner, Phys. Rev. C **71**, 064901 (2005).

[3] S. A. Bass *et al.*, Prog. Part. Nucl. Phys. **41**, 225 (1998).

[4] M. Bleicher *et al.*, J. Phys. G **25**, 1859 (1999).

[5] W. Cassing and E. L. Bratkovskaya, Phys. Rev. C **78**, 034919 (2008); Nucl. Phys. A **831**, 215 (2009).

[6] L. D. McLerran, R. Venugopalan, Phys. Rev. D **49**, 2233 (1994).

[7] V. K. Magas, L. P. Csernai, and D. D. Strottman, Phys. Rev. C **64**, 014901 (2001).

[8] I. N. Mishustin, J. Kapusta, Phys. Rev. Lett. **88**, 112501 (2002).

[9] B. Schenke, P. Tribedy, and R. Venugopalan, Phys. Rev. Lett. **108**, 252301 (2012).

[10] L.V. Gribov, E.M. Levin, M.G. Ryskin, Phys. Rept. **100**, 1 (1983).

[11] L. van Hove and S. Pokorski, Nucl. Phys. B **86**, 243 (1975).

[12] S. Raha, Physica Scripta T**32**, 180 (1990).

[13] E. Shuryak, Phys. Rev. Lett. **68**, 3270 (1992).

[14] J. Alam, S. Raha, and B. Sinha, Phys. Rev. Lett. **73**, 1895 (1994).

[15] T.S. Biró, E. van Doom, B. Müller, M.H. Thoma, and X.-N. Wang, Phys. Rev. C **48**, 1275 (1993).

[16] B. Kämpfer and O.P. Pavlenko, Z. Phys. C **62**, 491 (1994).

[17] B. Kämpfer, O. P. Pavlenko, A. Peshier, and G. Soff, Phys. Rev. C **52**, 2704 (1995).

[18] C.T. Traxler, M.H. Thoma, Phys. Rev. C **53**, 1348 (1996).

[19] D.M. Elliott, D.H. Rischke, Nucl. Phys. A **671**, 583 (2000).

[20] D. Dutta, S.V.S. Sastry, A.K. Mohanty, K. Kumar, and R.K. Choudhury, Nucl. Phys. A **710**, 415 (2002).

[21] F. Gelis, H. Niemi, R.V. Ruuskanen, S. S. Räsänen, J. Phys. G: Nucl. Part. Phys. **30**, S1031 (2004).

[22] F.-M. Liu and S.-X. Liu, Phys. Rev. C **89**, 034906 (2014).

[23] A. Monnai, Phys. Rev. C **90**, 021901 (2014).

[24] P. Moreau, O. Linnyk, W. Cassing, and E. Bratkovskaya, arXiv:1512.02875 [nucl-th].

[25] H. Stöcker *et al.* J. Phys. G: Nucl. Part. Phys. **43**, 015106 (2016).

[26] H. Stöcker *et al.*, Astron. Nachr. **336**, 744 (2015).

[27] V. Vovchenko, M. I. Gorenstein, L. M. Satarov, I. N. Mishustin, L. P. Csernai, I. Kisel, and H. Stöcker, Phys. Rev. C **93**, 014906 (2016).

[28] M. Strickland, Phys. Lett. B **331**, 245 (1994).

[29] K. Kajantie, M. Kataja, L. M. McLerran, and P.V. Ruuskanen, Phys. Rev. D **34**, 811 (1986).

[30] J. D. Bjorken, Phys. Rev. D **27**, 140 (1983).

[31] M. Ruggieri, S. Plumari, F. Scardina, and V. Greco, Nucl. Phys. A **941**, 201 (2015).

[32] S. Borsanyi, Z. Fodor, C. Hoelbling, S. D. Katz, S. Krieg, and K. K. Szabo, Phys. Lett. B **730**, 99 (2014).

[33] A. Bazavov (HotQCD Collaboration), Nucl. Phys. A **931**, 867 (2014).

[34] G. Boyd *et al.*, Phys. Rev. Lett. **75**, 4169 (1995).

[35] S. Borsanyi, G. Endrodi, Z. Fodor, S. D. Katz and K. K. Szabo, JHEP **1207**, 056 (2012).

[36] W. Broniowski, M. Rybczynski, and P. Bozek, Comput. Phys. Commun. **180**, 69 (2009).

[37] I. A. Karpenko, Y. M. Sinyukov, and K. Werner, Phys. Rev. C **87**, 024914 (2013).

[38] I. Karpenko, P. Huovinen, and M. Bleicher, Comput. Phys. Commun. **185**, 3016 (2014).

[39] B. Abelev *et al.* (ALICE Collaboration), Phys. Rev. C **88**, 044910 (2013).

[40] L. M. Satarov, I. N. Mishustin, A. V. Merdeev, and H. Stöcker, Phys. Atom. Nucl. **70**, 1773 (2007); Phys. Rev. C **75**, 024903 (2007).

[41] J.-F. Paquet *et al.*, arXiv: 1509.06738 [hep-ph].

[42] O. Linnyk, E. L. Bratkovskaya, W. Cassing, Prog. Part. Nucl. Phys. **87**, 50 (2016).

[43] D. Lohner [ALICE Collaboration], J.Phys.: Conf. Ser. **446**, 012028 (2013).

[44] P. Arnold, G.D. Moore, and L.G. Yaffe, JHEP **12**, 009 (2001).

[45] J. Ghiglieri, J. Hong, A. Kurkela, G.D. Moore, and D. Teaney, JHEP **05**, 010 (2003).

[46] J. Adam *et al.* [ALICE Collaboration], Phys. Lett. B **754**, 235 (2016).

[47] R. Chatterjee, H. Holopainen, T. Renk, and K. J. Eskola, Phys. Rev. C **85**, 064910 (2012).

[48] H. van Hees, M. He, and R. Rapp, Nucl. Phys. A **933**, 256 (2015).

[49] O. Linnyk, V. Konchakovski, T. Steinert, W. Cassing, and E. L. Bratkovskaya, Phys. Rev. C **92**, 054914 (2015).

[50] J. Kapusta, P. Lichard, D. Seibert, Phys. Rev. D **44**, 2774 (1991).

[51] R. Chatterjee, D.K. Shrivasta, T. Renk, Nucl. Phys. A **931**, 670 (2014).

[52] R. Chatterjee, D. K. Srivastava, H. Heinz, and C. Gale, Phys. Rev. C **75**, 054909 (2007).

[53] G. Vujanovic *et al.*, arXiv: 1602.01455.

[54] R.D. Pisarski, Nucl. Phys. B **309**, 476 (1988); Phys. Rev. Lett. **63**, 1129 (1989).

[55] F.D. Steffen and M.H. Thoma, Phys. Lett. B **510**, 98 (2001).

[56] G. N. Watson, *A treatese on the theory of Bessel functions*, Cambridge University Press, 1995, p. 415.